Acta Geotechnica
https://doi.org/10.1007/s11440-023-02123-9

RESEARCH PAPER

An investigation of the applicability of contact models to the normal load-deformation behaviour of artificially shaped granite

F. Altuhafi[1] · B. A. Baudet[1] · M. R. Coop[1]

Received: 11 July 2022 / Accepted: 28 October 2023

Abstract

The validity of different available contact models is tested against experimental data for contact normal loading of artificially shaped granite stones. Three elastic models and two plastic models were tested with different combinations of contact shape (spherical, conical and flat) and roughnesses. It was found that the deviation from the Hertz model increased with surface roughness with a generally better representation of the data achieved by using models which consider surface roughness and the fractality of the surface. The validity of all these models seems to be limited to before excessive plastic deformations start taking place, after which the contact seems to deform under constant stiffness.

Keywords Contact model · Contact stiffness · Particle surface roughness

List of symbol

a^*	Radius of area in contact for rough surfaces
a_H	Radius of the circle delimiting the contact surface
a_L	Radius of area in contact in Bahrami et al. [2] method
$a_L{}'$	Non-dimensional contact radius in Bahrami et al. [2] method
A_0	Area of contact at full yielding of asperities
d	Separation distance between the two nominal surfaces in contact
D_f	Fractal dimension
E^*	Combined modulus of elasticity of the two surfaces in contact
f	Normal force
F	Force at transition of behaviour from rough contact to Hertz
H	Hardness number
k	Normal stiffness
K_H^N	The Hertz normal stiffness
$K_{\mathrm{P\&P}}^N$	Normal stiffness as predicted by Pohrt and Popov [22]
N_H	Non-dimensional hardness parameter
N_L	Non-dimensional load parameter
p_0	Maximum contact pressure
P	Normal load
p'	Non-dimensional contact pressure by Bahrami et al. [2] method
$p_{0,H}$	Maximum pressure as predicted by Hertz
R_1, R_2	Radius of curvature for the two spheres in contact
R	Equivalent radius of curvature for the two surfaces in contact.
S_q	Root mean square of surface height
Z	Combined (elastic–plastic) vertical displacement of bulk and asperities, respectively,
Z^*	Dimensionless parameter of vertical displacement with respect to roughness
$\gamma(Z^*)$	Contact area fraction function
α	Non-dimensional roughness parameter
β	Radius of curvature of asperities peaks
δ	Mutual displacement at center of contact area
κ	Non-dimensional parameter in Bahrami et al. [2] method
η	Density of asperities per unit area
μ	Asperities shape parameter
ν	Poisson's ratio
σ	Combined RMS roughness
$\omega(0)$	Displacement caused from the elastically deformed bulk at the centre of the contact area

✉ F. Altuhafi
f.altuhafi@ucl.ac.uk

[1] Department of Civil, Environmental and Geomatics Engineering, University College London, London, UK

Published online: 26 November 2023

1 Introduction

It is generally accepted that the reliability of discrete element simulations of any granular material is significantly improved if the shape of the particles and the contact behaviour between them are properly characterised and modelled [11]. Several recent experimental studies (e.g. [5–8, 18]) have been carried out to that end, focusing on the contact between soil and rock particles under different modes of normal and tangential monotonic loading as well as cyclic normal loading. Their results highlighted important aspects of the grain scale response, suggesting parameters for DEM modelling such as contact stiffness and tangential friction coefficient that are different from what is typically used in numerical analyses.

Although a number of contact models are available and have been used in many applications in engineering, such as the Hertz elastic model [16], it is only in the last two decades, over which the discrete element method (DEM), [9], developed rapidly, that contact models applied to soils have come under scrutiny. The Hertz model, for example, was developed based on the assumption of contacting smooth spheres, while soil particles have irregular shapes and rough surfaces (e.g. [29]). The response at the contact may also not be fully elastic as assumed in most models (e.g. [4]). With methods of measurement for inter-particle contact behaviour and characterisation of particle morphology continuously improving, in parallel with more sophisticated contact models being developed, it has become possible to carry out a thorough investigation on the suitability of existing contact models for geo-materials. In this study, contact models, selected among the more appropriate ones available for granular soils, were reviewed and tested against data from normal loading tests between two artificially shaped granite particles. The tested particles were prepared to match the shapes for which the contact models were derived, i.e. with spherical or cylindrical contacting surfaces. By using input parameters directly measured on the tested material it was possible to evaluate the models' ability to capture the material response at the contact scale. This investigation using simple contact geometries was part of a large project aimed at producing an accurate DEM model of railway ballast. The interpretation of the tests on natural ballast were hampered by the complexity of the natural geometry at the contact, which prompted this series of tests on simple and controlled geometries.

Since the precursor elastic model for contact between two elastic smooth spheres presented by Hertz [16], developments have been made by others to account for the surface roughness of the majority of materials. Some models (e.g. [13–15]) proposed an extension to the Hertz model on the assumption that the asperities forming the surface roughness have spherical tips and deform elastically, while other models considered plastic deformation of the asperities (e.g. [2, 32]). The initial modification by Greenwood and Williamson [14] for contact between two rough flat surfaces assumed a Gaussian distribution of the asperities with an estimation of their radius of curvature. Similar assumptions were made by Greenwood and Tripp [13] to predict the contact behaviour of two rough spheres, but their model required the iteration of three integrals which led to complications in its application. Recognition that a less complicated model to use was necessary led Greenwood et al. [15] to apply a simpler statistical method relating the contact to a non-dimensional parameter representing the surface roughness, and which was the basis for an easy and practical solution proposed afterwards by Yimsiri and Soga [31] that has since been used in geotechnical DEM models (e.g. [28]). The limitation remains however that the body shapes at the contact and their surface characteristics should be easily quantifiable to be input directly in the models, as is the case in engineered materials.

Natural materials such as soils have no pre-defined geometry. They often have a complicated surface morphology resulting from complex geological history, and they differ from one type to another. A first step towards selecting the right contact model will be to simulate geo-materials of known contact shape and surface roughness: in this study this was achieved by choosing flat surfaces of the natural material. Particles were manufactured out of Mount Sorrel railway ballast which were cut into conical shapes or cut and milled into spheres before being tested using a bespoke inter-particle apparatus [27]. The mechanical properties of the material are known and the surface roughness of the spheres was measured before and after testing. As well as evaluating the selected models against the real contact data obtained from the contact tests, the nature of the normal force–displacement relationship is studied, limited to monotonic loading in this paper. The conclusions from this study should help extend the range of models typically used in DEM applied to soils, comparing different approaches and therefore suggesting how contact models for geo-materials may be further developed. Generally, the tests were stopped before major contact damage took place and catastrophic failure was usually avoided.

2 Experiments: material

Particles with defined geometry (spheres of different diameters, flat surfaces and conical shapes) were machined from a granodiorite ballast from Mount Sorrel. The mineralogy mainly consisted of plagioclase, potassium feldspar

and quartz [24]. The main mechanical properties of the Mount Sorrel granite are listed in Table 1 [1]. The Poisson's ratio used in the calculations was 0.25, a typical mean value for granite [10]. The choice of material was made based on the material used in a wider project to model the behaviour of railway ballast using DEM. Three UK universities (Nottingham University, University College London, UCL and the University of Southampton) were involved in this project, with UCL being tasked with providing the study of contact and micro-mechanical behaviour of the material.

The roughness of the spherical stones was controlled by using a stone polishing tumbler while the flaws in the flat surfaces were smoothed using polishing paper. A V8 Stereo-Discovery Microscope was used for surface image acquisition while analysis of the images was carried out using the ConfoMap7 software (equivalent to Mountains 7.4).

3 Experiments: apparatus

Data for the force–displacement relationships of surfaces in contact were obtained using the inter-particle apparatus designed at UCL and described in [27] (Fig. 1). The apparatus was developed to investigate the contact behaviour of coarse-grained materials, with vertical and horizontal capacities of 1 and 0.5 kN respectively. Two particles (stones) can be mounted on platens and subjected to loads along three axes that are concentric with the contact. In each axis, the load is applied by a linear actuator and measured with a load cell with a resolution of about 0.01–0.02 N. A non-contact displacement transducer along each axis is used to monitor the displacements with a resolution of 10^{-2} μm. The lower platen is held on a sled, under which is a three-point bearing system, for which the friction was calibrated, even if it was barely significant. A purpose written software that allows control of each axis in either a force or displacement mode is used to control the load application and to log the data during the test. To reduce compliance at the contact with the platen, the stones were cut flat on the side where they were attached to the platen by an epoxy resin, using a small thickness of glue to ensure minimum compliance. Although both normal and tangential loading can be applied to particles in this apparatus, the test data presented here are confined to normal loading to allow focus on the comparison with normal contact models. The datasets generated during the current study are available from the corresponding author on reasonable request.

Table 1 Mechanical properties of Mount Sorrel granite used in this study

Relative density	2.68
Unconfined compressive strength (MPa)	176.4
Poisson's ratio, ν	0.25
Young's Modulus (GPa)	60.6
Shore Hardness[a]	77 this is equivalent to 639 kg/mm^2 in Vicker's hardness[b]

[a]Shore Hardness is a measure of the resistance a material has to indentation. A diamond-tipped hammer is manually dropped vertically and freely from a height on to a horizontal, polished test surface

[b]The *Vickers hardness*, also referred to as a micro-hardness test, is carried out by observing the area of the indentation caused by a diamond pyramid indenter under vertical load

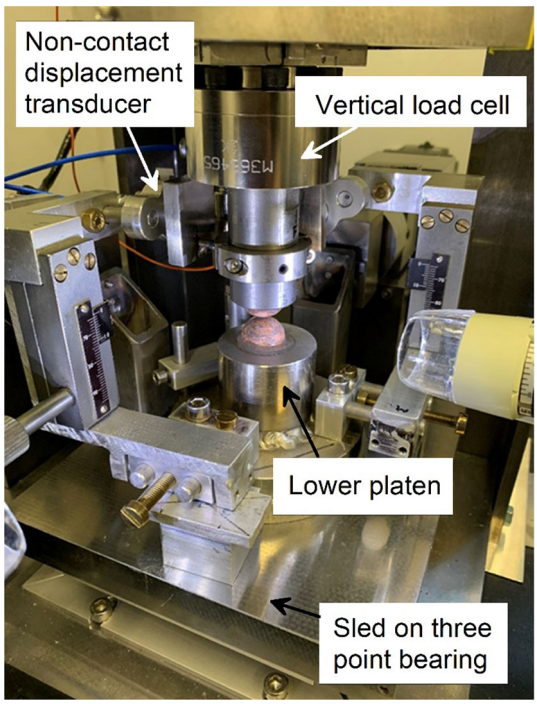

Fig. 1 Inter-particle loading apparatus during test SS(18–18) of two spheres with approximately similar diameter

Tests details are listed in Table 2. In all the tests, initial contact was made using a slow displacement control mode (0.1 mm/h) until the normal load reached 10 N, after which force control was started. This was done to avoid heavy impact between the two surfaces at first instant of contact had a force-controlled loading been used.

4 Roughness control and measurement

Geo-material surfaces contain irregularities of various orders ranging from shape deviations to irregularities of the order of interatomic distances. Measurement of surface roughness was done using a Zeiss Stereo-Discovery V8

Table 2 Test details for spherically shaped ballast

	Description	Measurements	Position of stone	
			Top stone	Lower stone
SS(18–18)	Smooth sphere–sphere test with approximate dimeters of 18–18 mm	Radius, mm	8.76	8.63
			Equivalent radius = 4.35	
		Roughness[a], μm	1.56	1.84
			Combined roughness = 2.40	
		D_f[b]	2.21	2.23
SS(12–18)	Smooth sphere–sphere test with approximate diameters of 12–18 mm	Radius, mm	6.05	8.75
			Equivalent radius = 3.58	
		Roughness, μm	2.83	3.09
			Combined roughness = 4.19	
		D_f	2.33	2.25
SF(12)	Sphere-flat test with approximate diameter 12 mm	Radius, mm	6.05	flat surface
			Equivalent radius = 6.05	
		Roughness, μm	3.61	5.48
			Combined roughness = 6.56	
		D_f	2.23	2.32
VS(18–18)	Very smooth sphere–sphere test with approximate diameter of 18–18 mm	Radius, mm	8.27	7.90
			Equivalent radius = 4.04	
		Roughness, μm	0.10	0.11
			Combined roughness = 0.15	
		D_f	2.06	2.09
RS(18–18)	Rough sphere–sphere test with approximate dimeters of 18–18 mm	Radius, mm	8.2	8.58
			Equivalent radius = 4.19	
		Roughness, μm	3.30	4.20
			Combined roughness = 5.34	
		D_f	2.17	2.23

[a]Roughness was calculated as the root mean square of the height of the surface

[b]Fractal dimension was calculated using box counting method

microscope. The roughness values reported in Table 2 are the root mean squares of surface height (RMS or S_q). Height measurements on the sample were made from Z-stack images obtained by the microscope using a magnification of 84×. The total area in view at the chosen magnification was 1.62 mm × 1.34 mm. Analysis of the scanned surface was done using the ConfoMap7 software, in which full analysis of the surface can be made to provide statistical data of the surface topography, for example by fractal analysis or peak analysis. The fractal dimension D_f, which gives an indication of the frequency of asperities to complement the RMS roughness, was calculated by ConfoMap 7 using the box counting method and is also given in Table 2. The values of surface roughness given in Table 2 were obtained after removing the effect of shape using a polynomial function in the ConfoMap7 software. Figure S1 in the supplementary documents illustrates the main procedure to obtain the surface roughness values followed in this study. When two rough surfaces come in contact, a combined roughness parameter σ is typically used in modelling calculations, where $\sigma = (S_{q1}^2 + S_{q2}^2)^{1/2}$, S_{q1} and S_{q2} representing the standard deviation of the asperity heights over a mean plane for the two surfaces in contact.

The size of the area considered in the roughness measurements was kept constant for consistent readings as it has been shown that the value of S_q can vary significantly depending on the size of the field of view. Roughness measurements were made before and after testing. Different initial surface roughnesses were achieved by means of a rock tumbler, obtaining roughness values ranging from 1.5 to 6 μm. Care was taken to measure the initial roughness where the area of contact was expected to take place, such as the apex in the case of a spherical shape, and to measure the roughness after applying different loads using the same field of view. Care was also taken that the area considered for the roughness measurements was consistent with the Hertz-predicted area for such contacts. It is the roughness

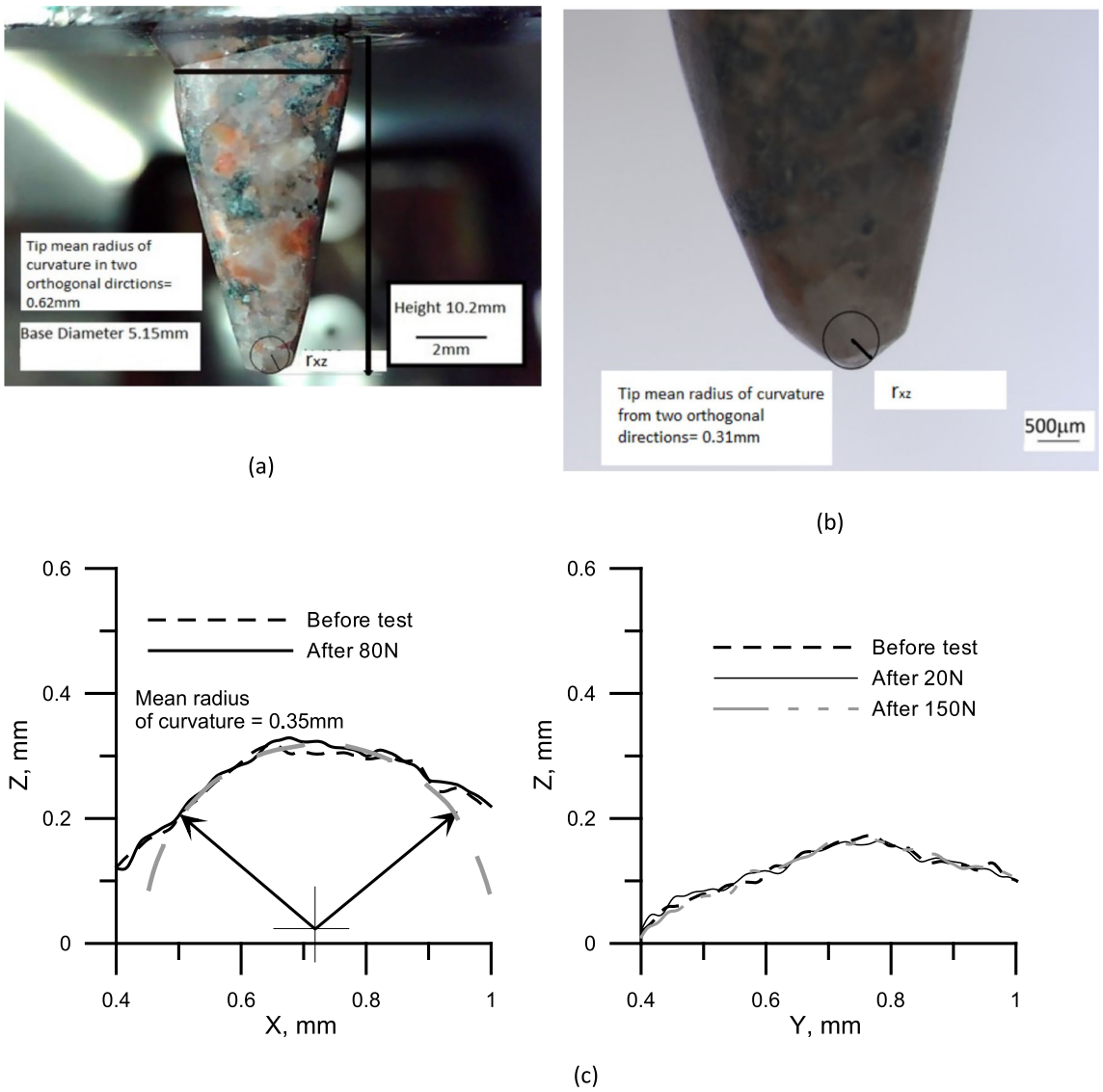

Fig. 2 Three different methods for radius of surface curvature estimation at the end of a cone tip **a** using digital camera **b** using profile images obtained by the microscope **c** using the Z-stack data of the surface as obtained by the microscope

within this area which could affect the contact behaviour. In this study, a field of view of 0.2 mm × 0.2 mm was chosen based on a Hertz prediction of the contact area between two spheres of 4.4 mm equivalent radius at about 100 N normal load. This calculated area reduces significantly with the decrease in the radius of curvature of the two surfaces in contact, e.g. for the tip of a conically shaped stone against a flat surface, the Hertz-predicted contact area radius is less than 0.09 mm at 100 N normal load.

The local shape of the area in contact should be considered when an estimation of radius of curvature at the contact is made. Figure 2 shows three different methods to estimate the radius of curvature of the cone in test FC5 using images which were obtained from: (1) two digital cameras, (2) profile images using the microscope and (3) profile data obtained from the Z-stack of the surface. The radius of curvature is determined in Fig. 2a, b by measuring the radius of the best fit circle at the tip of the cone and tangent to the bottom particle, as shown. In each method two orthogonal directions of the cone tip were considered. The camera set seems to capture the global shape and the curvature of the contact surface, yielding a much larger value of the contact radius R of about 0.62 mm compared to the other two methods with radii of 0.31 and 0.35 mm, respectively. This indicates the importance of image scale in estimating the surface properties for model evaluation and that using the microscope for smaller contact radius estimation is essential.

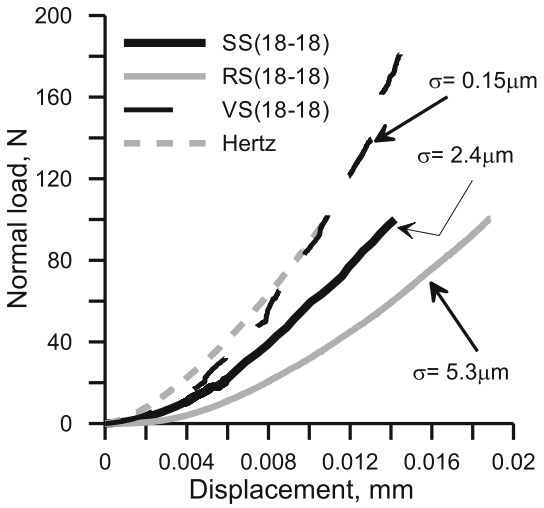

Fig. 3 Load–displacement response of three tests of sphere–sphere with similar equivalent radius but with different combined roughness values compared to Hertz model

5 Results and discussion: normal loading of spherically shaped particles

Five settings of tests on granite spheres, with different equivalent radii of curvature and different combined RMS roughnesses, were carried out as detailed in Table 2. Figure 3 shows the force–displacement response of three sphere–sphere contacts with similar curvature but with different surface roughnesses: a smooth pair of spheres SS(18–18), a very smooth sphere–sphere contact VS(18–18) and a rough pair of spheres RS(18–18), all subjected to normal loading. The spheres had a radius size in the range of 7.90–8.76 mm, with a calculated equivalent radius of 4.35 mm, 4.04 and 4.19 mm, respectively. The combined roughness of the spheres in RS(18–18) was more than twice the value for SS(18–18), while VS(18–18) was a very smooth set with a combined roughness value of 0.15 μm (see Table 2). The normal force–displacement relationships of these tests were compared with what is predicted by the Hertz model. The Hertz solution [16] was developed for normal contact between two smooth spheres treated as semi-infinite elastic bodies, and predicts that the radius of the circle delimiting the contact surface, a_H, is proportional to the cube root of the load level P (Eq. 1):

$$a_H = \left(\frac{3PR}{4E^*}\right)^{1/3} \tag{1}$$

If the modulus of elasticity and Poisson's ratio of the bodies in contact are (E_1, v_1) and (E_2, v_2) for the first and second sphere, respectively, the equivalent and combined parameters R and E^* for the two bodies in contact are:

- equivalent radius R with $1/R = 1/R_1 + 1/R_2$,
- combined elastic modulus E^* with $1/E^* = (1 - v_1^2)/E_1 + (1 - v_2^2)/E_2$.

The equations above for the equivalent or combined parameters were derived from the Hertz model based on effects of curvature and the elastic properties of the two surfaces in contact and cannot merely be obtained from the mean values of the individual parameters. The mutual displacement, δ, at the centre of the contact area, and the normal contact stiffness, $K_H^N (= dP/d\delta)$, obtained from the first derivative of load with respect to mutual displacement, can be calculated as:

$$\delta_H = \frac{a_H^2}{R} = \left(\frac{9P^2}{16RE^{*2}}\right)^{1/3} \tag{2}$$

$$K_H^N = \left(6PRE^{*2}\right)^{1/3} \tag{3}$$

In Fig. 3, the data for both tests SS(18–18) and RS(18–18) show a much softer response than the Hertz prediction, with the result for the rough contacting spheres RS(18–18) diverging the most. Test VS(18–18) which has an extremely low roughness value compared to the other two, however, shows a good agreement with the Hertz model. It is interesting that the effect of surface roughness is seen very clearly when compared with the predicted Hertz behaviour, even in the relatively smoother spheres of test SS(18–18), indicating a clear shortcoming of the model to predict an accurate behaviour for a material that is not perfectly smooth. This confirms the necessity of considering contact models that include roughness for a better representation of the data. In Fig. 3, the differences in displacements between the tests with various roughnesses are greater than the combined roughness indicated on the figure, but it must be recalled that the asperity peaks on the surfaces will be higher than the combined roughness.

While Eqs. (1)–(3) might be sufficient to predict the behaviour of almost smooth surfaces with an acceptable percentage of error, rough surfaces can exhibit significantly lower stiffnesses than predicted at low load levels due to the high error in estimating the real contact area [3, 15, 21]. For rough surfaces, initial contact takes place at the crest of the surface asperities over the nominal contact area, which is usually assumed by models to be larger than that predicted by Hertz for a smooth contact. It is important here not to confound the nominal contact area with the real contact area which is much smaller than this predicted by Hertz. Greenwood and Tripp [13] assumed that the asperities forming the surface roughness follow a Gaussian distribution, with asperity peaks having similar roundness and each asperity deforming individually according to the Hertzian law. Their model proved to be very complicated and required many iterations to reach a satisfactory result so further improvements and

simplifications followed. Greenwood et al. [15] suggested that the influence of the surface roughness on the accuracy with which the Hertz theory can predict the nominal contact area between spheres could be summarized in a non-dimensional roughness parameter α (Eq. 4), avoiding the need for an explicit statistical distribution of surface asperities:

$$\alpha = \frac{\sigma R}{a_H^2} \tag{4}$$

The parameter α gives an indication of the relative magnitudes of the asperities and the mutual displacement of the particles. The apparent nominal contact area between rough surfaces, a^*, is larger than that for smooth surfaces, and can be related to the Hertz model radius of contact area, a_H, by a function of the parameter α. It was found that for values of α less than 0.05, i.e. relatively smooth, Hertz theory under-estimates the nominal contact area radius by up to 7% [15], but at higher values of α, i.e. for rougher surfaces, a non-negligible increase in the apparent nominal contact area is observed. This is not to be confused with the real contact area which is likely to be much smaller for rough surfaces, which consists only of the smaller areas where the crests of the surface asperities are interacting. The pressure in these areas (or islands of contact) is therefore probably significantly higher than the contact pressure predicted by the Hertz model. This higher pressure will result in continuous deformation and yield of the surface asperities with increasing load until complete contact occurs, typically at high load, when the surface starts deforming following the Hertz stiffness, i.e. proportional to the load to the power 1/3 [18]. Johnson [17] estimated that yielding of a single asperity might occur at normal pressures of about 60% the material's hardness.

Using experimental data obtained by Greenwood et al. [15] from normal tests on hard steel spheres against flat surfaces, Yimsiri and Soga [31] proposed an expression to relate the ratio a^*/a_H to the roughness parameter α:

$$\frac{a^*}{a_H} = \frac{-2.8}{\alpha + 2} + 2.4 \tag{5}$$

The experimental data in Greenwood et al. [15] covered a range of α-values found for the metallic surfaces tested, up to unity, not reaching the higher values found in natural geo-materials with rougher surfaces and therefore it is not clear that Eq. (5) would be representative of the latter. When using Yimsiri and Soga's [31] equation, the mutual displacement is calculated from the Hertz Eq. (2), replacing a_H with a^*, and the stiffness can be derived from $dP/d\delta$ (see the appendix for full equation details). In the following this model with roughness added will be referred to as the RMS model.

There are very few comparisons between the normal contact behaviour of geo-materials with models in the literature. Full information about the surface morphology and curvature at the contact point is essential to be able to apply these models correctly. Yao et al. [30] compared data obtained from normal compression of a single quarzitic sand particle (Leighton Buzzard sand) against a hardened stainless steel platen with predictions by the Hertz model and by the RMS model. They found that the RMS model gives a better representation of the data, but that the behaviour tends to diverge from model predictions at higher loads, showing an even softer behaviour when plastic deformation of the bulk shape occurs at the contact, which in Yao et al.'s study [30] was quantified from examination of the particle morphology before and after the test by interferometry.

The RMS model, and Eq. (5) in particular, were tested against data obtained from experiments SS(18–18) and RS(18–18), described above, as well as a sphere-to-flat test SF(12) and a sphere-to-sphere test on two particles of different radii SS(8–12). This was achieved by back-calculating the rough contact area a^* from the test data assuming a Hertz load–displacement behaviour and plotting the ratio a^*/a_H against the calculated value of α based on the combined surface roughness and the Hertz displacement (Eq. 4). Similarly, the rough contact area was estimated for the quarzitic sand grains tested by [30]. The back-calculated data for the granite ballast and the quartz sand are plotted in Fig. 4 with the curve from Eq. (5). A theoretical solution for the contact of rough spheres had been developed by Greenwood and Tripp [13] who also

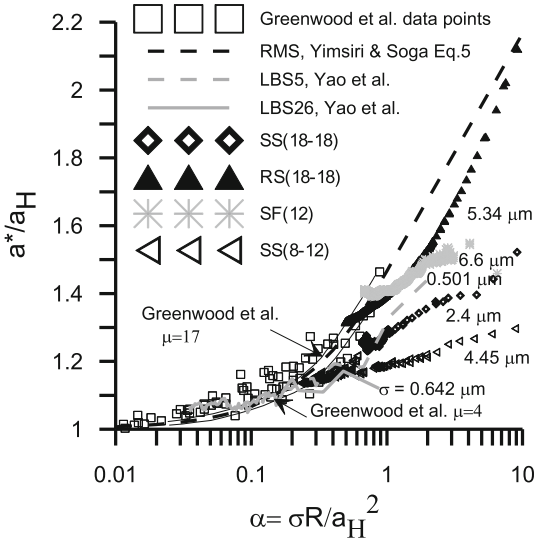

Fig. 4 Comparison of back-calculated tests data for geo-materials with Yimsiri and Soga [31] relationship (Eq. 5). Data of metal surfaces in contact as presented by Greenwood et al. [15] and the two curves of different μ values are also shown

considered the shape and distribution of asperities, captured in the parameter μ:

$$\mu = \frac{8}{3}\sigma\eta(2R\beta)^{1/2} \tag{6}$$

where η is the density of asperities per unit area and β is the radius of curvature of asperity peaks (assumed to be constant for each surface), and this is also shown in Fig. 4 for two values of μ ($\mu = 4$ and $\mu = 17$). It is clear that within the assumption of Hertzian deformation, the predicted effective contact radius for rough surfaces is significantly overestimated at larger values of α, although it is difficult to find a trend relating to the combined RMS roughness of the tested particles to the rate at which the ratio a^*/a decreases with decreasing α. This suggests that other factors not included in the parameter α, such as the shape of asperities or their density, may also influence the contact response. The larger α-values represent roughness-dominated behaviour, and at lower load levels the asperity deformation is predominant. Then as loading progresses and asperities are fully deformed the particles' mutual displacement becomes dominant and the value of α decreases towards zero, i.e. Hertz model behaviour.

6 The effect of surface self-affinity

Surfaces formed by random processes tend to be self-affine fractals (e.g. [19]), i.e. they look the same at different magnifications, but with different vertical and horizontal scales. Following Persson [20], improved methods to characterise natural rough surfaces that account for fractality have been proposed, for example by Yang et al. [28] for sands. These methods avoid the filters typically embedded in profiling software to separate roughness and local shape before calculating the root-mean-square roughness, which may not be suitable for non-engineered surfaces. Persson [21] proposed that contact occurs over many asperities, and that roughness does not have a single scale but changes with magnification. At high magnification the contact pressure at the asperities is so large that the material yields plastically and the size of the real contact area depends on the yield stress of the material. According to Persson's theory [20] the contact area increases linearly with the normal load as long as the true contact area is small compared to the apparent contact area.

A study by Pohrt and Popov [22] using the boundary element method for a finite indenter with a square area led to the following equation, relating the contact stiffness between self-affine surfaces to the normal force by an exponent that depends on the fractal dimension:

$$K^N_{\mathrm{P\&P}} = \frac{\pi\sqrt{A_0}E^*D_f}{10}\left(\frac{P}{\sigma E^*\sqrt{A_0}}\right)^{0.2567D_f} \tag{7}$$

where D_f is the fractal dimension of the surface, and A_0 is the area of contact when all asperities have yielded and full contact has taken place. In the case of contact between two rough spheres, this corresponds to the load when the two surfaces in contact start to deform following the Hertz model [23]. Pohrt and Popov [23] showed that rough spheres in contact can be treated as self-affine rough surfaces superimposed on smooth spheres. At levels of normal force too low to cause yielding of the asperities, the contact stiffness can be estimated using the self-affine rough surface model, i.e. Eq. (7). The Hertz model behaviour becomes applicable at higher forces. The main issue in applying this model is to find the load at which the transition from this model to Hertz occurs, i.e. when all asperities have yielded and the area A_0 can be calculated from the Hertz equations. This threshold load, and thus the full contact area A_0, can be found by solving the simultaneous equations based on the intersection of normal stiffness development with the applied normal load for these two models. To clarify this in an example, the Pohrt and Popov stiffness-load relation is plotted in Fig. 5 along with that from Hertz: the example shows the contact stiffness between two granite spheres SS(18–18), with equivalent radius 4.35 mm (for E and ν see Table 1), and an equivalent combined roughness of 2.40 µm. The predicted curves crossover at a normal load around 73 N, at which point the contact stiffness changes from following the self-affine

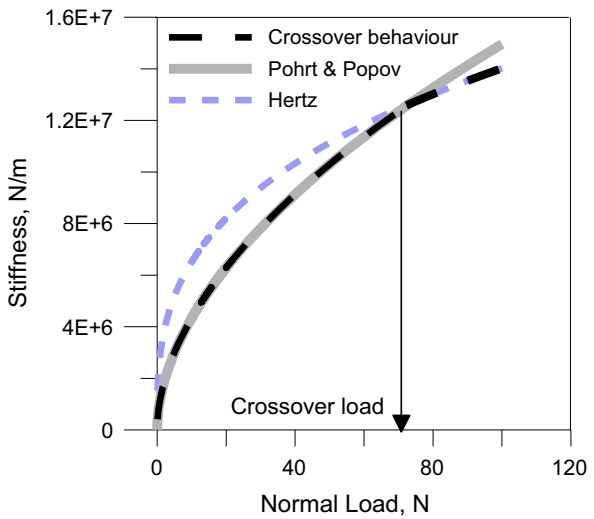

Fig. 5 Development of stiffness with normal load using Hertz model [16] and Pohrt and Popov model [22] for contact of two relatively rough granite spheres with equivalent radius $R = 4.35$ mm and $\sigma = 2.40$ µm

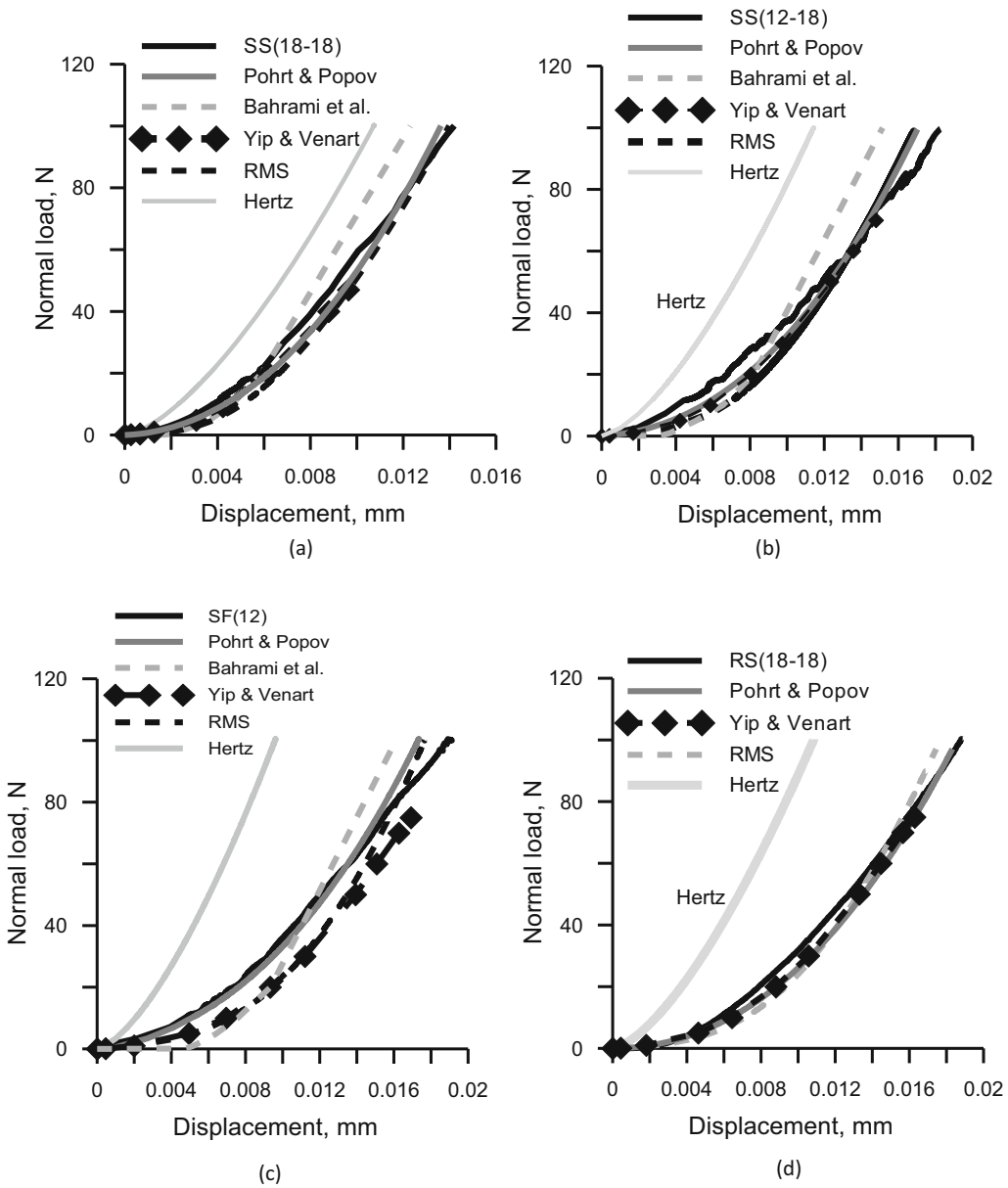

Fig. 6 Data for monotonic normal loading compared with various models **a** Test SS(18–18), **b** Test SS(12–18), **c** Test SF(12), **d** Test RS(18–18)

rough contact model (Pohrt and Popov) to the Hertz model stiffness. The threshold force at the crossover between the rough surface and the Hertz models, F, and the value of A_0, are calculated by:

$$A_0 = \frac{3}{4}\pi^{3/2} R\sigma \left(\frac{20}{\pi^{3/2} D_f}\right)^{1/0.2567 D_f} \tag{8}$$

$$F = \frac{4E^*}{3R}\left(\frac{A_0}{\pi}\right)^{3/2} \tag{9}$$

7 Plastic models

All the above mentioned models assumed pure elastic behaviour at the contact. Other modelling approaches adopted the idea of having a crust which is behaving plastically on an elastically deforming bulk. In this paper we review two of these models: the model presented by Yip and Venart [32] and the model proposed by Bahrami et al. [2, 3]. In both models, similar to what Greenwood and Trip [13] and Greenwood et al. [15] proposed, a Gaussian distribution of asperities is assumed. The nominal contact area is also assumed to extend beyond that predicted by the Hertz model. However, Yip and Venart built their model

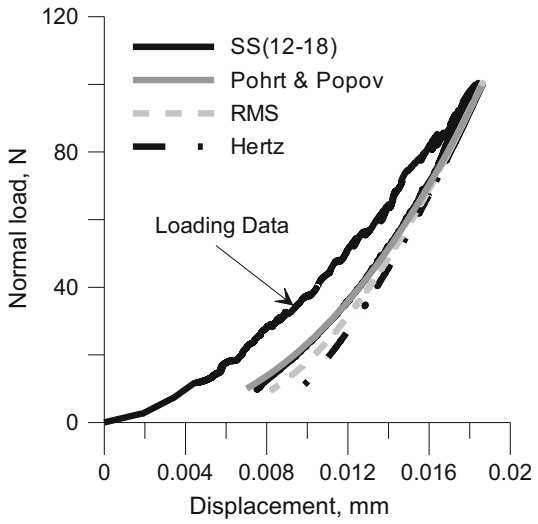

Fig. 7 Unloading data of Test SS(12–18) with three models: Hertz [16], RMS [31] and Pohrt and Popov [22]

on assuming that the real contact area is actually a fraction of the total nominal area in the rough contact.

Yip and Venart [32] suggested to treat the displacement of the elastic bulk and the plastically deforming crust separately, the asperities causing a separation distance between the two bulks. This separation distance (d) will reduce with the increasing contact force and the yielding process of the asperities until a complete yield of asperities has taken place, when the surfaces in contact start following a Hertz model behaviour and the normal stiffness will be equal to that predicted by Hertz model. The predicted displacement Z in this model is the outcome of the change in the separation distance d and the displacement caused from the elastically deformed bulk at the centre of the contact area $\omega(0)$ [32]. All distance variables in this model were made dimensionless by dividing them by the combined RMS roughness value, σ. The dimensionless separation distance d^* (= d/σ) is related directly to the contact area fraction (Z^*), which is the fraction of nominal contact area really interacting between the two surfaces which is a function of the dimensionless displacement Z^* (= Z/σ), and another two dimensionless variables, the load number N_L and the hardness number N_H:

$$N_L = \frac{2P}{\sigma E^* \sqrt{2R\sigma}};\ N_H = \frac{H}{E^* \sqrt{\sigma/8R}} \tag{10}$$

where H is either the Meyer's or Vicker's hardness number. Once the contact area fraction is related to the separation distance between the surfaces by the function γ (Z^*), the total expected real contact area can be obtained by integrating the areas of all the contact spots over the entire plane of contact. The real separation distance at each load can be found when the following relation is satisfied [32]:

$$N_L = 2\pi N_H \int_0^\infty \gamma(Z^*) r^* dr^* \tag{11}$$

where r^* is a dimensionless variable related to the horizontal distance from the centre of the nominal contact area r, the surface RMS roughness σ and the combined radius of the contacting surfaces R by the equation $r^* = r/\sqrt{2\sigma R}$. Equation (11) can be solved by iteration, choosing a set of possible separation distances and integrating over the range for r^*. It is noted that in spite of all the simplifications made to this model compared to the model proposed earlier by Greenwood and Trip [13], it is still difficult to derive a simple equation for the normal loading stiffness, as the above equation will not give a direct solution without going through the integral function and iteration. Predictions using Yip and Venart's [32] model are compared to the previous ones in Fig. 6.

Bahrami et al. [2, 3] also proposed a model to estimate the pressure distribution at rough surface contacts, with a similar assumption to Yip and Venart [32] of a plastic layer over an elastic body. They introduced the non-dimensional contact pressure $p' = p_0/p_{0,H}$, and the non-dimensional contact radius $a'_L = a_L/a_H$, where p_0 and a_L are the maximum pressure and radius of nominal contact area as predicted by Bahrami et al. model, while $p_{0,H}$ and a_H are the maximum pressure on the contact area and the contact area radius calculated using the Hertz model. The contact area is delimited by the perimeter where the contact pressure tends to zero. In their theoretical solution, Greenwood et al.'s [15] non-dimensional roughness parameter α is used to estimate the maximum contact pressure p_0' while the relationship between p_0' and the contact radius a_L in the Bahrami et al. model can be written explicitly:

$$p'_0 = \frac{1}{1 + 1.22\alpha\kappa^{-0.16}} \tag{12}$$

$$a'_L = \frac{a_L}{a_H} = \begin{cases} 1.605\sqrt{p'_0} & 0.01 \le p'_0 \le 0.47 \\ 3.51 - 2.51p'_0 & 0.47 \le p'_0 \le 1.0 \end{cases} \tag{13}$$

where κ is a nondimensional parameter equal to $(E^*\sqrt{R/\sigma})/H$, and the displacement is presented as a proportion of the displacement predicted by the Hertz model:

$$\frac{\delta}{\delta_H} = 0.5\left(a'_L\right)^2 + \frac{8p'_0 a'_L}{\pi^2\left[4.79 - 3.17\left(p'_0\right)^{3.13}\right]} \tag{14}$$

By substituting the appropriate relation in the above equation and differentiating the load with respect to the displacement ($dP/d\delta$), it is possible to obtain a set of two normal stiffness equations for this model depending on the

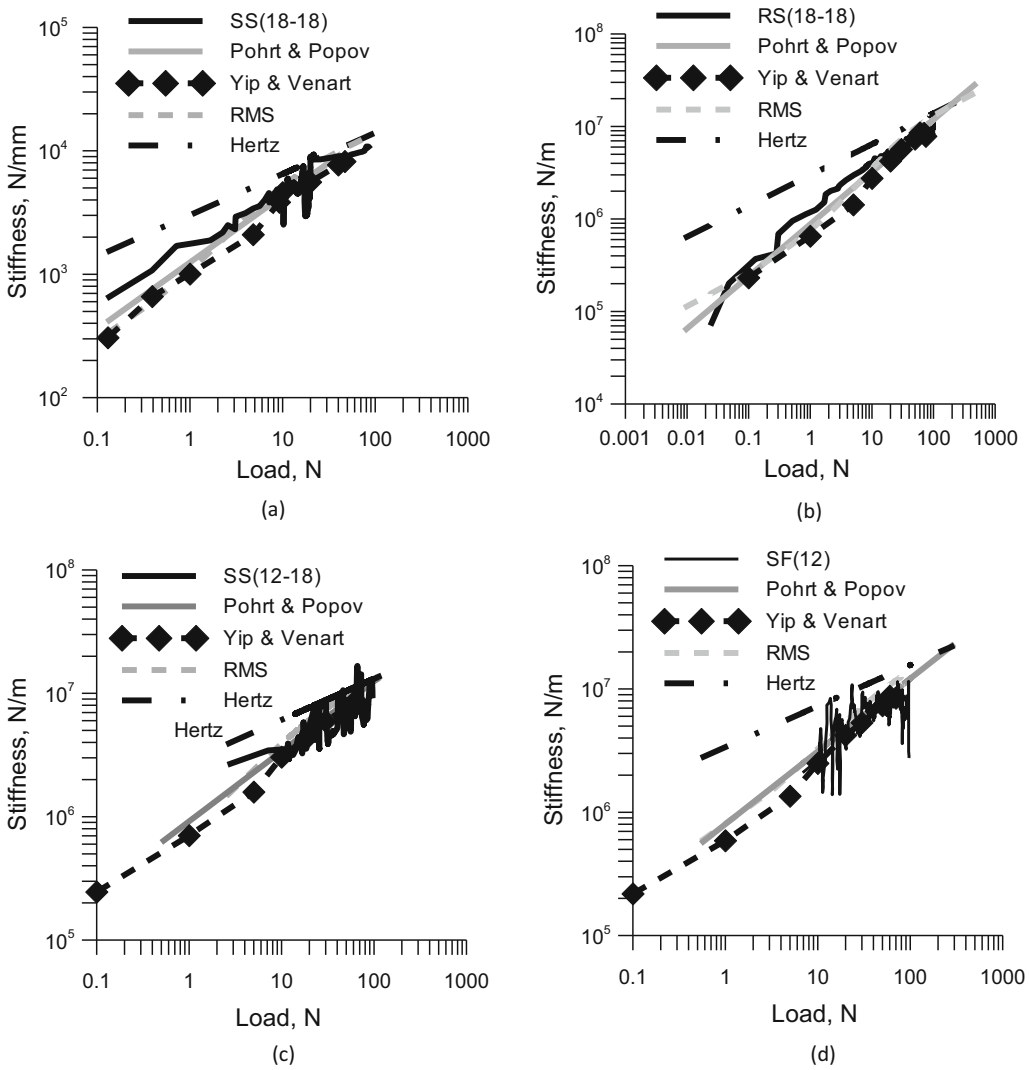

Fig. 8 Stiffness-load relationships obtained from experiments and as predicted by the four models **a** Test SS(18–18), **b** Test RS(18–18), **c** Test SS(12–18), **d** Test SF(12)

pressure range stated in Eq. (12). Predictions using Bahrami et al.'s model [3] are also compared to Hertz and other rough surface model predictions in Fig. 6.

8 Comparison between experimental data and predictions

Experimental data for sphere-to-sphere (SS(18–18), SS(12–18), RS(18,18)) and sphere-to-flat (SF(12)) contacts are compared with model predictions in Fig. 6 (test details in Table 2). For all of these tests, the Hertz model shows significantly stiffer behaviour in the testing load range (0–100 N). The simulated response is improved by using an estimated rough contact area in the elastic models, e.g. in the RMS model or by including fractality, e.g. affecting the stiffness exponent in the Pohrt and Popov model, but the good agreement ceases at higher loads (> 70 N) when the models predict a stiffer response than that observed for the real samples. The predictions by the plastic model proposed by Yip and Venart [32] on the other hand show a close fit to tests SS(18–18) and SS(12–18), i.e. for contact between smooth spheres, but too soft a response for test SF(12). Bahrami et al.'s [3] model does not seem to be suitable or is not applicable to any of the tested samples here. The observed behaviour during unloading, shown in Fig. 7 for SS(12–18), is stiffer so that using the Hertz model would be possible, as suggested by [25] in their elasto-plastic model. The predicted curves fit the test data better in the unloading stage, and for this particular test the Pohrt and Popov model shows the best agreement. It is interesting to note that modelling asperities as deforming elastically or plastically makes little difference to the fit.

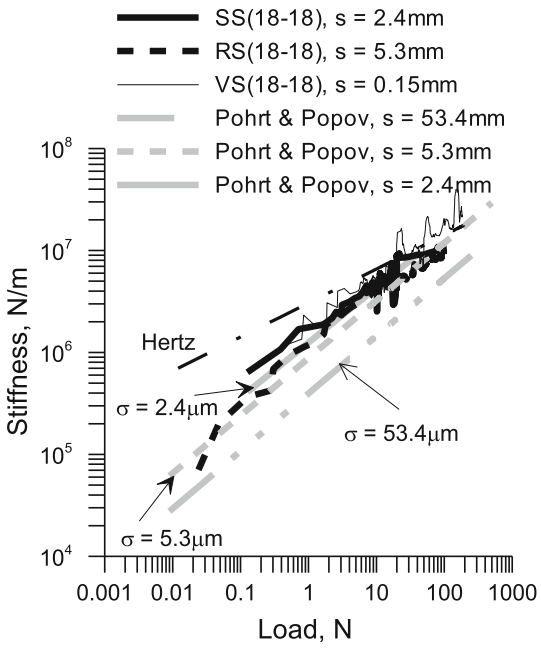

Fig. 9 Effect of roughness value on the predictions from the Pohrt and Popov model [22] applied to Tests SS(18–18) and RS(18–18). Experimental data of Test VS(18–18) and the predictions from the Hertz model [16] are also shown

However, no model includes plasticity of the bulk, which had been observed by [30].

Figure 8 compares the normal loading stiffnesses obtained from each test with those expected from the different models, plotted against normal load. There is a power law relation of stiffness with normal load in most contact models (e.g. [16, 21, 22]): the exponent is equal to 1/3 in the Hertz model, while it is linked to the surface roughness fractal dimension in the Pohrt and Popov model, equal to around 0.56 for the fractal dimensions of about 2.17–2.33 as tested here. A change in the combined root-mean-square roughness in the Pohrt and Popov model affects the position of the stiffness line by shifting it upwards or downwards, while the gradient stays the same (Fig. 9). Figure 9 also shows the change in stiffness with load of the three tests with similar ranges of equivalent radius: SS(18–18), RS(18–18) and VS(18–18). The very smooth set of spheres VS(18–18) exhibit the closest values among the three tests to the Hertz stiffness after the initial loading and even before reaching 10 N normal load.

Changes to the shape of the particles at the contact were monitored using the microscope. Figure 10 shows images of the top sphere of test RS(18–18) before and after compression, with the profiles plotted in Fig. 10b. No change to the bulk form was detected for the testing load range, so that plastic changes were limited to the roughness, observed at higher magnification in contrast to [30].

9 Normal compression of conically shaped ballast

Large degrees of curvature (i.e. small radii) can lead to plastic deformation of the bulk at the contact, in which case the elastic models do not apply anymore, even with roughness such as the RMS model [30]. In order to check the findings from Yao et al. [30], which were obtained from tests of quarzitic sand grains against a flat stainless steel surface, for the granite studied here particles were shaped into cones, i.e. with small radius spherical contacts. Although these conically shaped granite were sometimes a bit distorted due to difficulties in machining, the analysis presented here should not be affected as it is mainly dependant on the local shape or curvature at the point of contact which is usually accurately measured using microscopic images as was previously discussed and shown in Fig. 2. The cone-shaped particle RFC10, of mean radius of curvature of the tip of around 0.96 mm and RMS roughness of 5.04 μm, was subjected to cycles of loading–unloading to: 20, 40, 80, 150, 300 and 450 N against a flat surface, as shown in Fig. 11. Each cycle of loading–unloading resulted in substantial residual (plastic) deformations, increasing with load level. An important feature which can be seen in this test is the increase in stiffness during the reloading stages to values similar to those during unloading, exhibiting higher values than the stiffnesses during virgin loading. Modelling of the load–displacement curve with the elastic models RMS and Pohrt and Popov was only possible to loads up to 20 N, as shown clearly in Fig. 11b, after which no model can fit the obtained data for higher loads. This can be due to significant plastic deformation taking place for loads more than 20 N. Figure 12 shows the change in stiffness with load level for each stage of loading during Test RFC10. The first loading (RFC1–20 N) is well simulated by the Pohrt and Popov model. As expected from the load–displacement response, reloading stages exhibit a much higher stiffness up to gross yield, almost equivalent to the Hertz stiffness, before the stiffness drops down to an apparently constant value of around 5000 N/mm. The cumulative plastic deformations during the test are plotted against the maximum normal load reached for each stage in Fig. 13. A nearly linear relationship can be seen with normal load.

Test FC5, a cone-flat contact using a cone with a diameter of 5 mm (i.e. smaller radius), also consisted of multiple stages of cyclic loading/unloading to different normal load levels (Table 3) but the surface deformation was monitored between stages by removing the sample from the apparatus for imaging in between stages of loading. Although care was taken to put the cone back in position so that the same area of the flat surface was

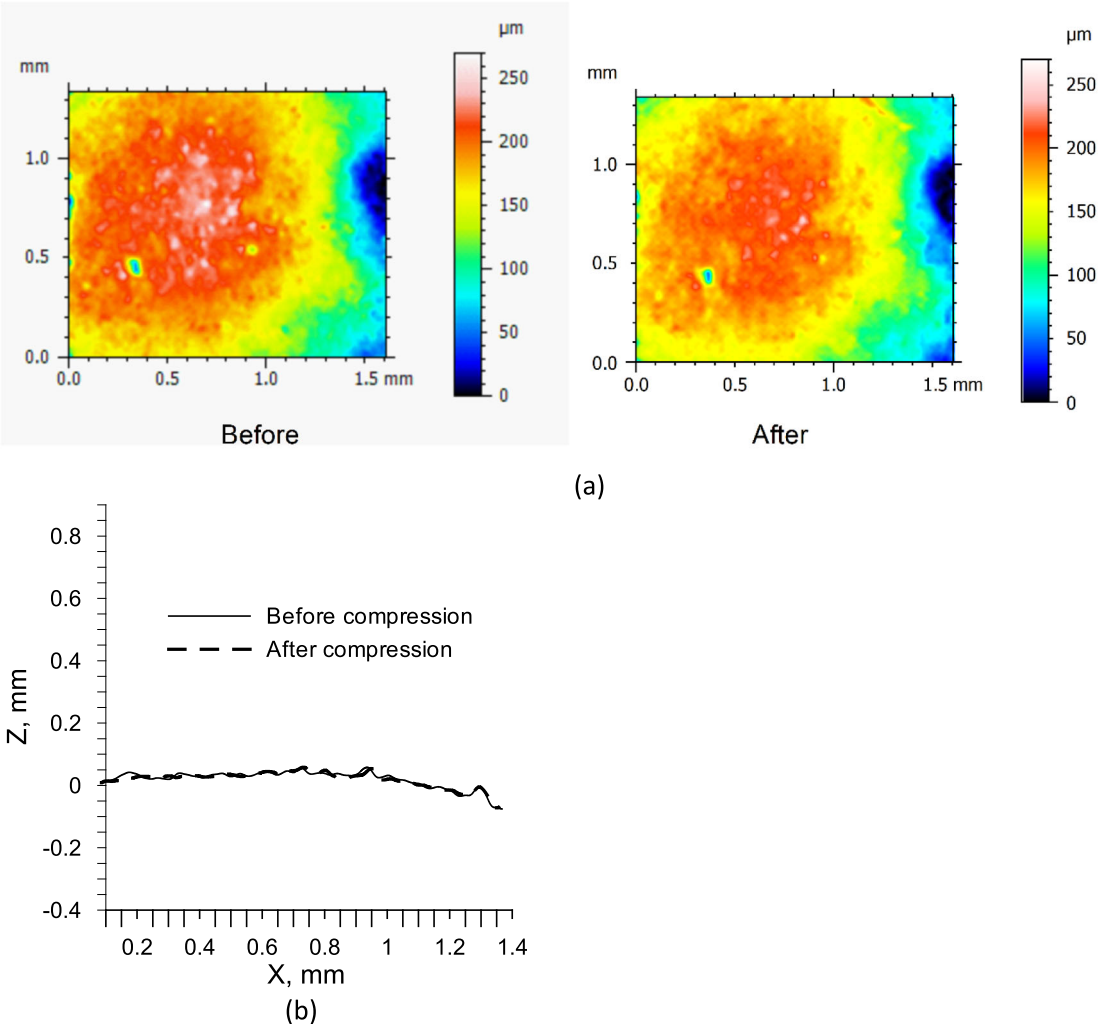

Fig. 10 The surface of the top sphere from Test RS(18–18) before and after compression **a** height map, **b** lateral profile section

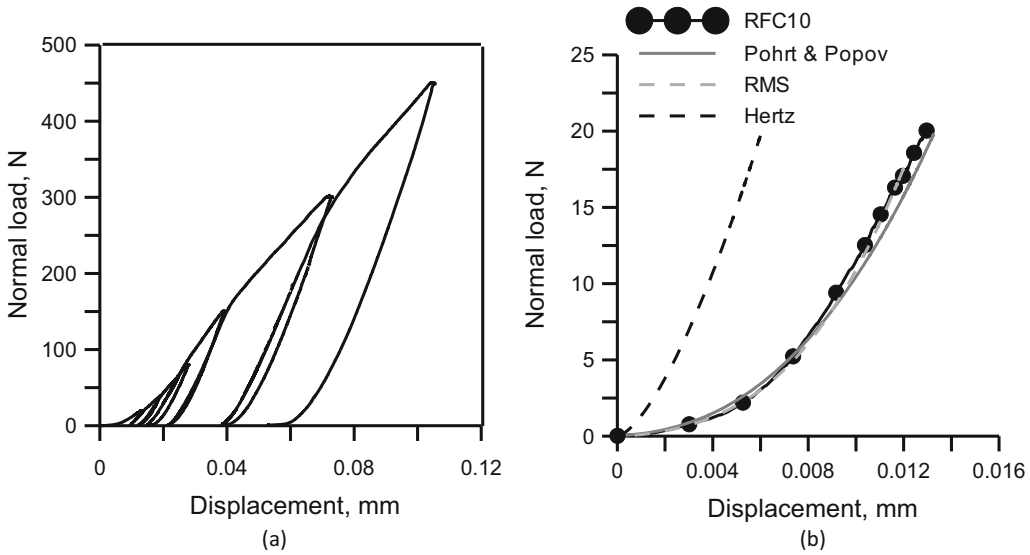

Fig. 11 Load–deformation relationship during Test RFC10. **a** loading/unloading **b** initial load to 20 N compared to three elastic models: Hertz [16], RMS [31] and Pohrt and Popov [22]

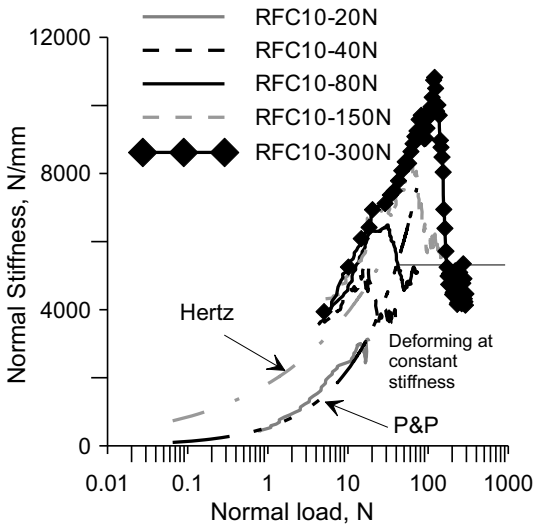

Fig. 12 Normal loading stiffnesses during loading stages of Test RFC10

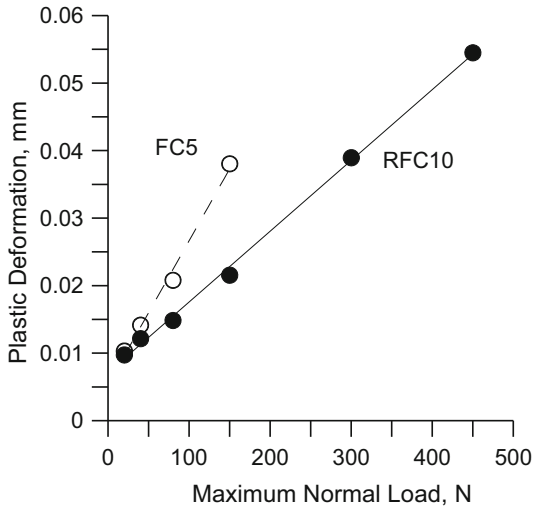

Fig. 13 Cumulative plastic deformation during Tests RFC10 and FC5

reloaded, it was not possible to ensure the exact same point was used in the successive stage. It is therefore very likely that each stage started with a new contact point. When plotting the data in Fig. 14, the displacement of each stage is shown as starting from zero. The first stage included a single cycle of normal loading to 20 N followed by unloading, while the second stage consisted of two cycles of loading/reloading to 20 and 40 N and the third is carried out by three cycles of loading/unloading and so on till the fifth and final stage to 150 N (Fig. 14a–d). Model predictions, limited to the Hertz, RMS and Pohrt and Popov models, are compared with data from the first and second stages of loading to 20 N in Fig. 14a. The experimental data of the first and second stages up to 20 N show high consistency in response between the different stages. The Hertz model predicts a much stiffer response than observed from the data. A good fit with the Pohrt and Popov model is observed at normal loads less than 7 N, while the RMS model tends to overestimate the value of deformation at low levels of loading, as was shown earlier. The test data, however, diverge from the rough surface models at loads larger than 7 N, exhibiting a much stiffer behaviour. This may be due to the initiation of plastic deformation at the contact which happens in this test at even lower loads than noted in RFC10 (20 N), indicating that plastic deformation for this contact with a significantly smaller radius is taking place at loads as low as 7 N considering that these models are for an elastic deformation for both the bulk shape of the contact area and surface deformations. The plastic deformations during the different stages of loading for this test also compare well with the values noted for test RFC10 in Fig. 13.

The surface morphology of the cone and the flat surface (Test FC5) was examined before and after each stage up to the 150 N loading stage. No significant change of the cone tip bulk shape was noted with most of the deformation taking place in the flat surface, similarly to what was found in test RFC10, and the flat surface suffered most of the plastic deformation. Test FC5 was taken up to 225 N normal load, where a catastrophic cone tip failure occurred. The load–displacement curve then showed multiple failure points before reloading to reach the maximum load of 300 N (Fig. 14e). All the unloading stages for cone-flat contacts including this one, showed a stiff behaviour.

The good fit of elastic models that include surface roughness, such as the RMS and Pohrt and Popov models, with the experimental data seems to be limited to cases when there is no or limited deformation of the bulk shape at the contact, i.e. usually for very low normal loads. This was also found by Yao et al. [30] for quartz sand subjected to compression against a flat platen. Models that assume plastic deformation of the crust, e.g. by Yip and Venart [32] can only successfully predict the contact behaviour when the plastic deformation is not significant at the contact. However, as the radius of curvature decreases, i.e. for smaller contact areas such as at the cone tip, plastic deformation becomes more pronounced and extends to the bulk shape of the contact with the consequence that these models stop being in agreement with the test data. This supports a need to consider plastic deformations in the contact behaviour, especially at higher loads. The fact that most models which adopt elastic solutions yield a power relation between normal force and normal stiffness [12, 16, 22] should also be considered. While the Hertz model with its stiffness power law exponent of 1/3 produced a higher stiffness than those observed in rough surfaces at low loads, Goddard [12] suggested a transition

from a relationship $k \propto f^{1/2}$ at lower loads, where k is the normal stiffness and f the normal load, to the Hertz relationship $k \propto f^{1/3}$ at higher loads. This follows a transition of contact geometry from a sharp contact at lower loads to a more rounded contact which will follow the Hertz model at higher loads. The stiffness values produced according to this method might be very similar to those that can be produced by the Pohrt and Popov model [22] which considers both the surface roughness and the surface fractality at the contact, although the concept here is very different to that adopted by Goddard [12]. The power value for the Pohrt and Popov model before full contact takes place between the two surfaces and the transition to the Hertz model is dependent on the surface fractal number. Goddard's [12] hypothesis on the other hand would not be compatible with the sudden decrease in stiffness upon yielding, where again a plastic formulation may be more suitable.

The experimental observations presented in this study were implemented in a DEM model by Tolomeo and McDowell [26] who adopted the Pohrt and Popov model for first loading and Hertz for unloading, thereby giving a plastic component of displacement. This was applied to the simulation of small strain stiffness probes on ballast in a large triaxial cell. Preliminary results of the simulations showed a significant change in small strain stiffness, that can be attributed to the different contact normal stiffness between the rough surface model and the classic Hertz model.

10 Conclusions

Capturing the right behaviour of geo-materials in DEM requires accurate modelling of the material mechanical behaviour in terms of the contact load-deformation and stiffness during different modes of loading. The irregular shapes and surfaces of the geo-material makes this even harder as most available models are built on specific shapes and known surface finish. Spherical and conical stones with

Table 3 Test details for conically shaped tests

Test	RFC10	FC5
Description	Cone against flat	Cone against flat
	Cut ballast surface in multiple cycles of load/unload to 20, 40, 80, 150 and 300 N without removing sample between cycles	Cut ballast surface in multiple cyclic loading stages with sample surface morphology monitoring between stages. Five stages were conducted:
		1st: load to 20 N then unload
		2nd: load/unload to 20 N then 40 N
		3rd: load/unload to 20, 40 and 80 N
		4th: load/unload to 20, 40, 80 and 150 N
		5th: load/unload to 20,40, 80, 150 and up to failure load
Base diameter mm	10.75	5.15
Cone height mm	10.97	9.90
Tip curvature radius[a] mm	0.96	0.32
Surface roughness[b] S_q µm	5.04	3.67
Fractal dimension[c] D_f	2.66	2.05
Flat surface: S_q µm	2.47	1.95
Flat surface: D_f	2.17	2.02

[a]Radius was obtained from profile images in two orthogonal directions

[b]Roughness was calculated as the root mean square of the height of the surface

[c]Fractal dimension was calculated using box counting method

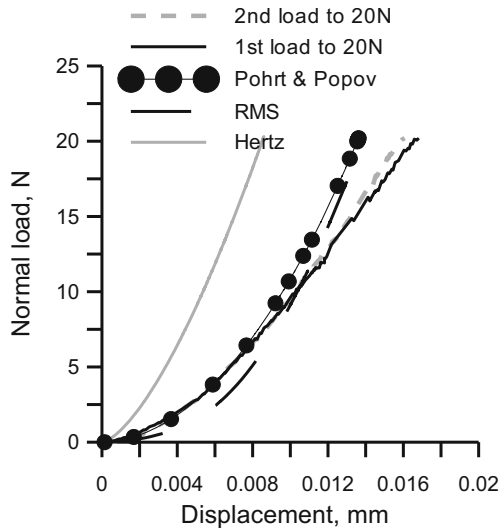
2nd load to 20N
1st load to 20N
Pohrt & Popov
RMS
Hertz
Normal load, N
Displacement, mm
0
5
10
15
20
25
0
0.004
0.008
0.012
0.016
0.02

(a)

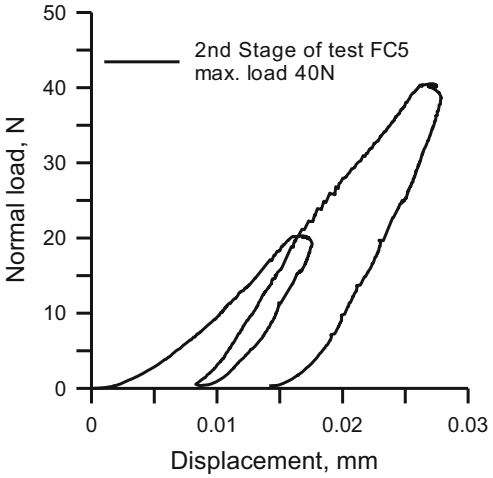
2nd Stage of test FC5
max. load 40N
Normal load, N
Displacement, mm
0
10
20
30
40
50
0
0.01
0.02
0.03

(b)

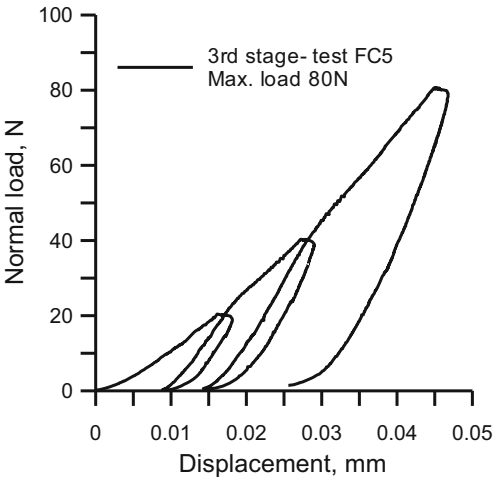
3rd stage- test FC5
Max. load 80N
Normal load, N
Displacement, mm
0
20
40
60
80
100
0
0.01
0.02
0.03
0.04
0.05

(c)

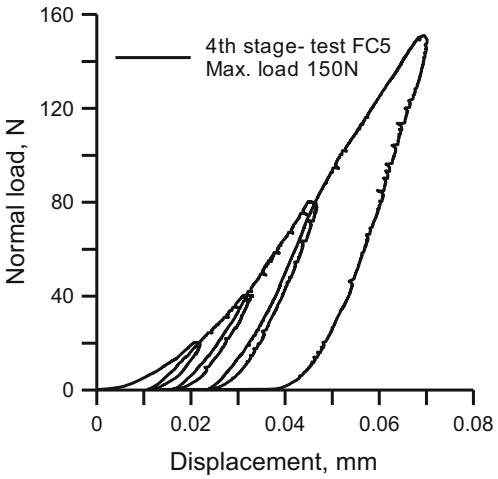
4th stage- test FC5
Max. load 150N
Normal load, N
Displacement, mm
0
40
80
120
160
0
0.02
0.04
0.06
0.08

(d)

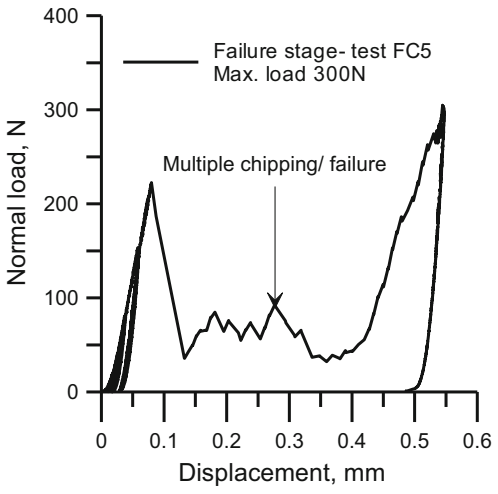
Failure stage- test FC5
Max. load 300N
Multiple chipping/ failure
Normal load, N
Displacement, mm
0
100
200
300
400
0
0.1
0.2
0.3
0.4
0.5
0.6

(e)

◀**Fig. 14** Stages of cyclic loading/unloading in Test FC5 **a** First load/unload stage to 20 N normal load compared to the second stage loading to the same normal load with three different contact models, **b** Second stage load/unload to 20 and 40 N, **c** Third stage load/unload to 20, 40 and 80 N, **d** Fourth stage load/unload to 20, 40, 80 and 150 N, **e** The 5th and final stage of test FC5 showing multiple cone tip failure displacement-load relationship

controlled surface roughness which were machined of ballast were used in this study to examine the behaviour of the material during normal loading. The normal loading behaviour was tested against different contact models. Below are the main points can be drawn from this study:

1. The Hertz model in general was unable to capture the behaviour of the material for the tested load range apart from the smoothest surfaces (Test VS(18–18)). The best fit for spherically shaped ballast was seen with the elastic model which considers the self-affinity (fractality) of the surface, Pohrt and Popov [22] and the plastic model proposed by Yip and Venart [32].
2. The stiffness of the contact decreases with the increase in surface roughness. The effect of surface roughness is very significant at lower load levels. When the applied normal load is large enough to cause a complete yield of the asperities in the crust, the sample stiffness follows the Hertz model stiffness [18]. This was not seen here in the presented data except for the very smooth contact in Test VS(18–18). In fact the significant plastic deformations, as in the case of smaller radii of curvature in conical contact tests, resulted in a constant stiffness deformation region at higher loads.
3. The equation which was proposed by Yimsiri and Soga [31] to determine the normal contact area of rough surfaces generally leads to an overestimation of deformation at lower load levels. This might be because the effect of surface morphology features such as the distribution and shape of peaks/asperities have a more pronounced effect at this load level, which the equation does not consider.
4. Reloading of contact is associated with higher stiffnesses, which drop to the initial virgin loading stiffness after reaching the maximum load previously reached. However, when the contact suffers from excessive plastic deformation which extends to its bulk shape, the contact starts to deform with constant stiffness.
5. Plastic deformation is noted to take place during normal loading even at modest loads when the contact has small radii and high curvature. This plastic deformation is proportional to the maximum load reached for the cones studied here.

Appendix

From Hertz theory:

$$a = \left[\frac{3(1-v)R\,P_N}{4G}\right]^{1/3}$$

where a is the contact area radius, R is the equivalent radius, P_N is the normal load, v is Poisson's ratio, G is the shear modulus.

From Greenwood et al. [13], the roughness parameter α can be calculated from the equation:

$$\alpha = \frac{\sigma R}{a^2} = 2\sigma\left(\frac{2RG^2}{9(1-v)^2P_N^2}\right)^{1/3}$$

where σ is the combined roughness of the two surfaces in contact.

Yimsiri and Soga [30] proposed an equation to relate α with the ratio of contact area radius of rough surfaces a^* to the Hertzian contact area as in the equation below:

$$\frac{a^*}{a} = \frac{-2.8}{\alpha+2} + 2.4$$

Substituting α and a equations in the proposed equation:

$$a^* = \left(\frac{-2.8}{2\sigma\left[\frac{2RG^2}{9(1-v)^2P_N^2}\right]^{1/3}+2} + 2.4\right) \cdot \left[\frac{3(1-v)R\,P_N}{4G}\right]^{1/3}$$

$$\delta = \frac{a^{*2}}{R} = \frac{1}{R}\left(\frac{-2.8}{2\sigma\left[\frac{2RG^2}{9(1-v)^2P_N^2}\right]^{1/3}+2} + 2.4\right)^2 \cdot \left[\frac{3(1-v)RP_N}{4G}\right]^{2/3}$$

Let $M = \frac{G^2}{(1-v)^2} = E^{*2}$; where E^* is the equivalent elastic modulus with $1/E^* = (1-{v_1}^2)/E_1 + (1-{v_2}^2)/E_2$

$$\delta = \frac{1}{R}\left(\frac{-2.8}{2\sigma\left[\frac{2MR}{9P_N^2}\right]^{1/3}+2} + 2.4\right)^2 \cdot \left[\frac{9R^2P_N^2}{16M}\right]^{1/3}$$

We then differentiate δ with respect to P_N:

To start differentiation: let $H = \left(\frac{2MR}{9}\right)^{1/3}$

$$\delta = \underbrace{\left(\frac{-2.8}{2\sigma H P_N^{-2/3}+2}+2.4\right)^2}_{A} \cdot \underbrace{\frac{P_N^{2/3}}{2H}}_{B}$$

$$A' = 2\left(\frac{-2.8}{2\sigma H P_N^{-2/3}+2}+2.4\right) \cdot \left(\frac{-2.8 * \left(\frac{4}{3}\right)\sigma H P_N^{-5/3}}{\left(2\sigma H P_N^{-2/3}+2\right)^2}\right)$$

$$A' = \frac{1568\sigma H P_N^{-5/3}}{75.\left(2\sigma H P_N^{-2/3}+2\right)^3} - \frac{448\sigma H P_N^{-5/3}}{25.\left(2\sigma H P_N^{-2/3}+2\right)^2}$$

$$B = \frac{P_N^{2/3}}{2H}; B' = \frac{P_N^{-1/3}}{3H}$$

Now: $d\delta = AB' + A'B$

$$\frac{d\delta}{dP_N} = \left(\frac{-2.8}{2\sigma H P_N^{-2/3}+2}+2.4\right)^2 \cdot \frac{P_N^{-1/3}}{3H} + \frac{P_N^{2/3}}{2H}\left(\frac{1568\sigma H P_N^{-5/3}}{75.\left(2\sigma H P_N^{-2/3}+2\right)^3} - \frac{448\sigma H P_N^{-5/3}}{25.\left(2\sigma H P_N^{-2/3}+2\right)^2}\right)$$

The normal stiffness is therefore:

$$\frac{dP_N}{d\delta} = \left[\left(\frac{-2.8}{2\sigma H P_N^{-2/3}+2}+2.4\right)^2 \cdot \frac{P_N^{-1/3}}{3H} + \frac{P_N^{2/3}}{2H}\left(\frac{1568\sigma H P_N^{-5/3}}{75.\left(2\sigma H P_N^{-2/3}+2\right)^3} - \frac{448\sigma H P_N^{-5/3}}{25.\left(2\sigma H P_N^{-2/3}+2\right)^2}\right)\right]^{-1}$$

Supplementary Information The online version contains supplementary material available at https://doi.org/10.1007/s11440-023-02123-9.

Acknowledgements The authors would like to express their gratitude to Mr Ben Boorman and Mr Matthew Wilkinson, technical staff at the Soil Mechanics laboratory at University College London. The authors would also like to thank Dr Ting Yao, from the Institute of Rock and Soil Mechanics, Chinese Academy of Sciences, Wuhan, China, for kindly making some of her data available for comparison. This research was fully funded by the EPSRC grant number EP/S026460/1, in collaboration with Professor G.R. McDowell at Nottingham University and Dr A. Zervos at Southampton University.

References

1. Afrouz A (1992) Practical handbook of rock mass classification systems and modes of ground failure. CRC Press, Boca Raton
2. Bahrami M, Culham JR, Yovanovich MM, Schneider G (2004) Thermal contact resistance of nonconforming rough surfaces, part 1: contact machanics model. J Thermophys Heat Transf 18:209–217
3. Bahrami M, Yovanovich MM, Culham JR (2005) A Compact model for spherical rough contacts. J Tribol 127(4):884–889
4. Cavarretta I, Coop MR, O'Sullivan C (2010) The influence of particle characteristics on the behaviour of coarse grained soils. Géotechnique 60(6):413–423
5. Cavarretta I, Rocchi I, Coop MR (2011) A new interparticle friction apparatus for granular materials. Can Geotech J 48(12):1829–1840
6. Cole DM, Peters JF (2007) A physically based approach to granular media mechanics: grain-scale experiments, initial results and implications to numerical modeling. Granul Matter 9(5):309
7. Cole DM, Peters JF (2007) Grain-scale mechanics of geologic materials and lunar simulants under normal loading. Granul Matter 10(3):171
8. Cole DM, Mathisen LU, Hopkins MA, Knapp BR (2010) Normal and sliding contact experiments on gneiss. Granul Matter 12(1):69–86
9. Cundall PA, Strack ODL (1979) A discrete numerical model for granular assemblies. Géotechnique 29(1):47–65
10. Domede N, Parent T, Sellier A (2017) Mechanical behaviour of granite. A compilation, analysis and correlation of data from around the world. Eur J Environ Civ Eng 23(2):1–19
11. Ferellec J, McDowell G (2010) Modelling realistic shape and particle inertia in DEM. Géotechnique 60(3):227–232
12. Goddard JD (1990) Nonlinear elasticity and pressure-dependent wave speeds in granular media. Proc Math Phys Sci R Soc 430(1878):105–131
13. Greenwood JA, Tripp JH (1967) The elastic contact of rough spheres. J Appl Mech 34(1):153–159
14. Greenwood JA, Williamson JBP (1966) Contact of nominally flat surfaces. Proc R Soc Lond A 295:300–319
15. Greenwood JA, Johnson KL, Matsubara E (1984) A surface roughness parameter in Hertz contact. Wear 100(1):47–57
16. Hertz H (1881) Über die Berührung fester elastischer Körper. J für die reine und angewandte Mathematik 92:156–171
17. Johnson K (1985) Contact mechanics. Cambridge University Press, Cambridge
18. Nardelli V, Coop MR (2019) The experimental contact behaviour of natural sands: normal and tangential loading. Géotechnique 69(8):672–686
19. Nayak PR (1971) Random process model of rough surfaces. J Lubr Technol 93(3):398–407
20. Persson BNJ (2001) Elastoplastic contact between randomly rough surfaces. Phys Rev Lett 87:116101

21. Persson BNJ (2006) Contact mechanics for randomly rough surfaces. Surf Sci Rep 61(4):201–227
22. Pohrt R, Popov VL (2012) Normal contact stiffness of elastic solids with fractal rough surfaces. Phys Rev Lett 108(10):104301
23. Pohrt R, Popov VL (2013) Contact mechanics of rough spheres: crossover from fractal to Hertzian behavior. Adv Tribol 974178
24. Scott PW, Rollinson GK (2015) Crushed rock aggregates: their mineralogy and textures using automated scanning electron microscopy. In: Hunger E, Brown TJ (eds) Proceedings of the 18th extractive industry geology conference, 2014. EIG Conferences, pp 49–68
25. Thornton C, Ning Z (1998) A theoretical model for the stick/bounce behaviour of adhesive, elastic-plastic spheres. Powder Technol 99(2):154–162
26. Tolomeo M, McDowell GR (2022) Implementation of real contact behaviour in the DEM modelling of triaxial tests on railway ballast. Powder Technol 412:118021
27. Wong C, Coop MR (2020) Development of inter-particle friction in a railway ballast. Géotechnique Lett 10:535–541
28. Yang J, Dai BB (2011) DEM analysis of soil fabric effects on behaviour of sand. Géotechnique 61(8):715–719
29. Yang H, Baudet BA, Yao T (2016) Characterization of the surface roughness of sand particles using an advanced fractal approach. Proc R Soc A 472:20160524
30. Yao T, Baudet BA, Lourenço SDN (2021) Evolution of surface roughness of single sand grains with normal loading. Géotechnique 72(6):543–555
31. Yimsiri S, Soga K (2000) Micromechanics-based stress–strain behaviour of soils at small strains. Géotechnique 50(5):559–571
32. Yip FC, Venart JES (1971) An elastic analysis of the deformation of rough spheres, rough cylinders and rough annuli in contact. J Phys D Appl Phys 4(10):1470–1486